

Impacts of Hurricane Irma (2017) on ocean transport processes

Thomas Dobbelaere^{a,*}, Milan Curcic^b, Matthieu le Hénaff^{c,d}, Emmanuel Hanert^{a,e}

^a*Eath and Life Institute (ELI), UCLouvain, Louvain-la-Neuve, Belgium*

^b*Rosenstiel School of Marine and Atmospheric Sciences (RSMAS), University of Miami, Coral Gables, Florida, USA*

^c*Cooperative Institute for Marine and Atmospheric Studies (CIMAS), University of Miami, Miami, Florida, USA*

^d*Atlantic Oceanographic and Meteorological Laboratory (AOML), NOAA, Miami, Florida, USA*

^e*Institute of Mechanics, Materials and Civil Engineering (IMMC), UCLouvain, Louvain-la-Neuve, Belgium*

Abstract

In most hydrodynamic model studies, currents and waves are simulated in an uncoupled manner.*[connection not very clear]* This is especially true for the simulation of passive tracers, whose trajectories are often computed based solely on currents. Although this simplification holds for most situations, as the force exerted by waves on currents can be neglected in fair weather conditions, it may lead to significant errors during storm conditions, when currents are strongly influenced by wind-generated waves. In this study, we investigate current-wave interactions in heavy-wind conditions by coupling the unstructured-mesh hydrodynamic model SLIM with the spectral wave model SWAN. We apply the coupled model in the Florida Reef Tract during Hurricane Irma (Sep. 2017) and show that it successfully reproduces both the observed wave behavior and storm surge during the passage of the hurricane. The modeled currents are then used to simulate the trajectories of passive

*Corresponding author

Email address: thomas.dobbelaere@uclouvain.be (Thomas Dobbelaere)

drifters during the passage of the hurricane. Our results show that taking wave force into account induces variations of up 1 m/s in modelled currents on the continental shelf break as well as in the vicinity of reefs and islands. Wave-current interactions can therefore deflect the trajectories of drifting material by up to 10 km on the passage of the storm **Add something?**. These results strongly advocate for the inclusion of wave forces while studying transport processes (sediments, pollutants, larvae, etc.) in heavy-wind conditions.

Keywords:

1. Introduction

Wave-current interactions in coastal areas are of great importance for coastal engineering as they play a key role in sediment transport, morphological evolution and pollutant mixing (Bever and MacWilliams, 2013; Li and Johns, 1998). However, these interactions are highly nonlinear and can vary significantly in space and time (Wu et al., 2011). Wave-induced currents are generated by wave radiation stress gradients (Longuet-Higgins, 1970), affecting water levels near shorelines and wave breaking points (Longuet-Higgins and Stewart, 1964). Changes in water levels and currents, in turn, affect the motion and evolution of the waves (Sikirić et al., 2013). Coupled wave-current models are therefore required to capture these complex interactions.

As coastal oceans are characterized by complex topology with islands, inlets and estuaries, unstructured (usually two-dimensional) models are preferred as structured grid models show limitations in resolving topologically-controlled nearshore processes (Wu et al., 2011; Chen et al., 2007). [Transition needed here] The effect of wave-interactions becomes even more significant in the case of hurricanes, that generate large wind-waves and disturb ocean conditions (Liu et al., 2020) by causing coastal upwellings on continental shelves (Smith, 1982) and inducing strong currents, waves and storm surges in nearshore and coastal regions (Dietrich et al., 2010; Weisberg and Zheng, 2006).

South Florida and the Gulf of Mexico are particularly vulnerable to

22 hurricanes (Malmstadt et al., 2009) and modelling studies predict tropical
23 cyclones to increase both in frequency and intensity in this region (Marsooli
24 et al., 2019; Knutson et al., 2010). Being able to accurately model wave-current
25 interactions in this area becomes thus critical. *Expand...*

26 Individual-based modelling of particulates has been extensively used to
27 study the transport of drifting materials such as pollutants, sediments or
28 larvae (Le Hénaff et al., 2012; Liubartseva et al., 2018; Figueiredo et al.,
29 2013; Frys et al., 2020). Although some of these studies take the impact of
30 waves into account by adding a Stokes drift velocity, *i.e.* the net drift of a
31 floating particle in the direction of the wave propagation (Van Den Bremer
32 and Breivik, 2018), to the Eulerian currents, they usually neglect the wave-
33 induced currents. Such practice is reasonable in the case of fair weather,
34 when wave-induced forces exerted on currents are relatively small, but might
35 lead to significant inaccuracies during storm conditions (Röhrs et al., 2012;
36 Curcic et al., 2016). To assess the importance of wave-current interactions
37 during a tropical cyclone, we investigated the transport of drifting particles
38 on the Florida shelf during Hurricane Irma, one of the strongest and costliest
39 tropical cyclones on record in the Atlantic Basin (Xian et al., 2018), which
40 made landfall in Florida in September 2017.

41 In this study, we developed an unstructured coupled wave-current model of
42 South Florida to simulate the ocean circulation during hurricane Irma. Both
43 modelled currents and waves were validated against field measurements and
44 were then used to simulate the transport of drifting material in the Florida
45 Keys and the Florida inner shelf during the storm. Model outputs were then
46 compared with uncoupled simulation results in order to assess the impact of
47 wave-induced forces and Stokes drift on the modelled currents and transports.

⁴⁸ **2. Methods**

⁴⁹ *2.1. Study area and observational data*

⁵⁰ Large-scale ocean circulation around South Florida is dominated by the
⁵¹ Florida Current (FC), which originates from the Loop Current (LC) where it
⁵² enters the Florida Straits from the Gulf of Mexico, and, downstream, forms
⁵³ the Gulf Stream. The FC is a major western boundary current characterized
⁵⁴ by spatial variability and meandering, associated with the presence of cyclonic
⁵⁵ eddies between the core of the current and the complex reef topography of the
⁵⁶ Florida Reef Tract (FRT) (Lee et al., 1995; Kourafalou and Kang, 2012). The
⁵⁷ northern half of these reefs are made of early Holocene reef frameworks and
⁵⁸ indurated sand ridges while the southern part (the Florida Keys) is composed
⁵⁹ of a chain of limestone islands, fossilized remnants of ancient coral reefs and
⁶⁰ sand bars (Hoffmeister and Multer, 1968; Shinn, 1988; Lidz and Shinn, 1991).
⁶¹ The variability of the FC extends over a large range of spatial and temporal
⁶² scales, with periods of 30-70 days in the Lower Keys (Lee et al., 1995) and
⁶³ shorter periods of 2-21 days in the Upper Keys (Lee and Mayer, 1977), and
⁶⁴ exhibits significant seasonal and interannual cycles (Johns and Schott, 1987;
⁶⁵ Lee and Williams, 1988; Schott et al., 1988). Circulation on the West Florida
⁶⁶ Shelf (WFS) on the other hand is forced by local winds and tidal fluctuations
⁶⁷ (Lee and Smith, 2002; Liu and Weisberg, 2012).

⁶⁸ The state of the ocean around Florida is monitored by an extensive
⁶⁹ array of tide gauges, current meters and buoys. In this study, we used sea
⁷⁰ surface elevation measurements from the National Oceanic and Atmospheric
⁷¹ Administrations (NOAA) Tides and Currents dataset. These measurements
⁷² were taken at four locations: two in the Florida Keys (Key West and Vaca Key);
⁷³ one on the eastern coast of Florida (Virginia Key); and one on the western
⁷⁴ coast (Naples). For the currents, we used ADCP measurements from the
⁷⁵ University of South Florida's College of Marine Science's (USF/CMS) Coastal
⁷⁶ Ocean Monitoring and Prediction System (COMPS) for the WFS (Weisberg
⁷⁷ et al., 2009). More specifically, we used measurements from moorings C10,

⁷⁸ C12 and C13, respectively located at the 25, 50, and 50 m isobaths of the
⁷⁹ WFS (Liu et al., 2020). Finally, for the waves, we used measurements from
⁸⁰ four buoys of the NOAA's National Data Buoy Center (NDBC); two on
⁸¹ Florida's Eastern shelf and two on the WFS. The locations of all measurement
⁸² stations are shown on Fig. 1A,C.

⁸³ *2.2. Wind and atmospheric pressure during Hurricane Irma*

⁸⁴ Irma made landfall in Florida on 10 September 2017 as a category 3
⁸⁵ hurricane, first at Cudjoe Key (Florida Keys) and later on Marco Island,
⁸⁶ south to Naples (see hurricane track in Fig. 1). It then weakened to a
⁸⁷ category 2 hurricane as it moved further inland (Pinelli et al., 2018). The
⁸⁸ storm damaged up to 75% of the buildings at his landfall point in the Florida
⁸⁹ Keys, making it one of the strongest and costliest hurricanes on record in the
⁹⁰ Atlantic basin (Xian et al., 2018; Zhang et al., 2019). The strongest reported
⁹¹ wind speed was 50 m/s on Marco Island while the highest recorded storm
⁹² surge was 2.3 m, although larger wind speed likely occurred in the Florida
⁹³ Keys (Pinelli et al., 2018) In order to reproduce the wind profile of Irma in
⁹⁴ our model, we used high-resolution H*Wind wind fields (Powell et al., 1998)
⁹⁵ *[add figure to compare H*Wind and ERA-5]*. As these data represent 1-min
⁹⁶ averaged wind speeds, we multiplied them by a factor 0.93 to obtain 10-min
⁹⁷ averaged wind speeds (Harper et al., 2010), which are more consistent with
⁹⁸ the time step of our model. Furthermore, H*Wind wind profiles did not cover
⁹⁹ the whole model extent during the passage of the hurricane and were thus
¹⁰⁰ blended within coarser wind field extracted from ECMWF ERA-5 datasets.
¹⁰¹ Pressure fields of Irma were also constructed using ERA-5 data. However, the
¹⁰² coarse resolution of the dataset smooth out the depression at the center of
¹⁰³ the hurricane, leading to an underestimation of the pressure gradient in our
¹⁰⁴ model. To better capture the central depression of Irma, we built a hybrid
¹⁰⁵ pressure field using the position and the minimal pressure of the core of the
¹⁰⁶ hurricane based on its track as recorded in the HURDAT 2 database (Landsea
¹⁰⁷ and Franklin, 2013). Based on this information, the hybrid pressure field

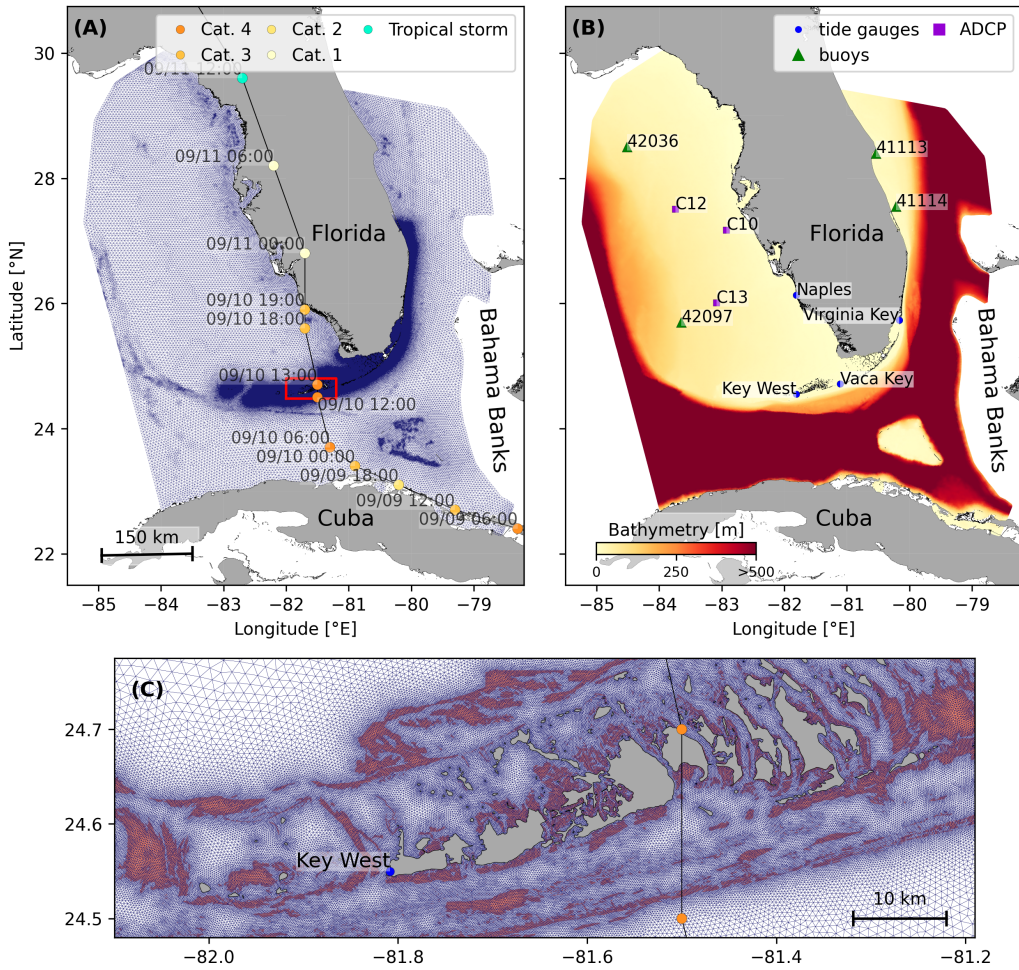


Fig. 1: **A:** Mesh of the computational domain with the trajectory of Irma, category of the hurricane is given by the Saffir-Simpson color scale. **B:** Bathymetry of the domain with the location of stations used for the validation of the model outputs. **C:** Close up view of the Lower Keys area, where the mesh resolution reaches 100m near reefs (shown in dark orange) and islands (highlighted in dark grey)

108 was constructed by combining an idealized Holland pressure profile (Lin and
 109 Chavas, 2012) within the radius of maximum wind speed of Irma (Knaff et al.,
 110 2018) with ERA-5 pressure field. The transition between from the Holland
 111 profile to ERA-5 data outside the radius of maximum wind speed data was
 112 performed using a smooth step function [*add a figure to visualize that*].

113 *2.3. Hydrodynamic model*

114 Ocean currents generated during hurricane Irma around South Florida
 115 were modelled using the 2D barotropic version of the unstructured-mesh
 116 coastal ocean model SLIM¹. The model mesh covers an area similar to the
 117 model extent of Dobbelaere et al. (2020b), that includes the FRT but also the
 118 Florida Straits and part of the Gulf of Mexico (Figure 1). However, this area
 119 has been slightly extended northeastward and westward in order to include
 120 the NOAA-NDBC buoys. Furthermore, to withstand potential cell drying
 121 during the hurricane, we solved the conservative shallow water equations with
 122 wetting-drying:

$$\begin{aligned}
 \frac{\partial H}{\partial t} + \nabla \cdot (\mathbf{U}) &= 0 , \\
 \frac{\partial \mathbf{U}}{\partial t} + \nabla \cdot \left(\frac{\mathbf{U}\mathbf{U}}{H} \right) &= -f\mathbf{e}_z \times \mathbf{U} + \alpha g H \nabla(H - h) - \frac{1}{\rho} \nabla p_{\text{atm}} + \frac{1}{\rho} \boldsymbol{\tau}_s \quad (1) \\
 &\quad + \nabla \cdot (\nu \nabla \mathbf{U}) - \frac{C_b}{H^2} |\mathbf{U}| \mathbf{U} + \gamma (\mathbf{U}_{\text{ref}} - \mathbf{U}) ,
 \end{aligned}$$

123 where H is the water column height and \mathbf{U} is the depth-averaged transport;
 124 f is the Coriolis coefficient; g is the gravitational acceleration; h is the
 125 bathymetry; α is a coefficient stating whether the mesh element is wet ($\alpha = 1$)
 126 or dry ($\alpha = 0$) [*add more detail about impact of wetting-drying ?*]; ν is the
 127 viscosity; C_b is the bulk bottom drag coefficient; ∇p_{atm} is the atmospheric
 128 pressure gradient; $\boldsymbol{\tau}_s$ is the surface stress, usually due to wind; and γ is a
 129 relaxation coefficient towards a reference transport \mathbf{U}_{ref} . As in Frys et al.

¹<https://www.slim-ocean.be>

¹³⁰ (2020) and Dobbelaere et al. (2020b), SLIM currents were gradually relaxed
¹³¹ towards the operational Navy HYCOM product (GOMI0.04², Chassignet et al.
¹³² (2007)) in regions where the water depth exceeds 50m.

¹³³ At very high wind speeds, the white cap is blown off the crest of the waves
¹³⁴ (also known as spumes), which has been hypothesized to generate a layer
¹³⁵ of droplets that acts as a slip layer for the winds at the ocean-atmosphere
¹³⁶ interface (Holthuijsen et al., 2012). This causes a saturation of the wind drag
¹³⁷ coefficient for strong winds (Donelan et al., 2004; Curcic and Haus, 2020;
¹³⁸ Powell et al., 2003). To account for the impact of this saturation on the surface
¹³⁹ wind stress in our model, we implemented the wind drag parameterization of
¹⁴⁰ Moon et al. (2007). In this parameterization, the drag coefficient C_d depends
¹⁴¹ on the wind speed at 10-m height U_{10} according to:

$$C_d = \kappa^2 \log \left(\frac{10}{z_0} \right)^{-2} \quad (2)$$

¹⁴² where κ is the von Karman constant. The roughness length z_0 in Eq. (2) is
¹⁴³ expressed as:

$$z_0 = \begin{cases} \frac{0.0185}{g} U_*^2 & \text{if } U_{10} \leq 12.5 \text{ m/s ,} \\ [0.085(-0.56U_*^2 + 20.255U_* + 2.458) - 0.58] \times 10^{-3} & \text{if } U_{10} > 12.5 \text{ m/s ,} \end{cases} \quad (3)$$

¹⁴⁴ with U_* the friction velocity. The relation between U_{10} and U_* is given by:

$$U_{10} = -0.56U_*^2 + 20.255U_* + 2.458 . \quad (4)$$

¹⁴⁵ The mesh resolution depends on the distance to coastlines and reefs
¹⁴⁶ following the approach of Dobbelaere et al. (2020b). The mesh is then further
¹⁴⁷ refined according to bathymetry value and gradient, as suggested in the

²<https://www.hycom.org/data/gom10pt04>

148 SWAN user-guide³. Such an approach improves the model efficiency as the
 149 mesh resolution is only increased where required by the currents and waves
 150 dynamics. The mesh was generated with the seamsh⁴ Python library, which is
 151 based on the the open-source mesh generator GMSH (Geuzaine and Remacle,
 152 2009). It is composed of approximately 7.7×10^5 elements. The coarsest
 153 elements, far away from the FRT, has a characteristic length of about 5 km
 154 whereas the finest elements have a characteristic length of about 100 m near
 155 coastlines and reefs (Fig 1).

156 *2.4. Wave model*

157 Waves were modelled using the parallel unstructured-mesh version of the
 158 Simulating WAves Nearshore (SWAN) model (Booij et al., 1999), one of the
 159 most commonly used wave models in coastal areas and inland waters. This
 160 model solves the action balance equation (Mei, 1989):

$$\frac{\partial N}{\partial t} + \nabla_{\mathbf{x}} \cdot [(\mathbf{c}_g + \mathbf{u})N] + \frac{\partial}{\partial \theta}[c_\theta N] + \frac{\partial}{\partial \sigma}[c_\sigma N] = \frac{S_{in} + S_{ds} + S_{nl}}{\sigma}, \quad (5)$$

161 where $N = E/\sigma$ is the wave action density and E is the wave energy spectrum;
 162 θ is the wave propagation direction; σ is the intrinsic wave frequency; \mathbf{c}_g is
 163 the wave group velocity, $\mathbf{u} = \mathbf{U}/H$ is SLIM depth-averaged current velocity;
 164 c_θ and c_σ are the propagation velocities in spectral space due to refraction
 165 and shifting in frequency due to variations in depth and currents; and S_{in} ,
 166 S_{ds} , and S_{nl} respectively represent wave growth by wind, wave decay and
 167 nonlinear transfers of wave energy through interactions between triplets
 168 and quadruplets. Spectra were discretized with 48 direction bins and 50
 169 frequency bins logarithmically distributed from 0.03 to 2 Hz. Exponential
 170 wind growth was parameterized using the formulation of Janssen (1991),
 171 while dissipations by whitecapping and bottom dissipations followed the

³<http://swanmodel.sourceforge.net/unswan/unswan.htm>

⁴<https://pypi.org/project/seamsh/>

172 formulations of Komen et al. (1984) and Madsen et al. (1989), respectively.
 173 Coefficients for exponential wind growth and whitecapping parameterizations
 174 were based on the results of Siadatmousavi et al. (2011), and significantly
 175 differ from SWAN's default settings. By default, SWAN implements the
 176 wind input formulation of Komen et al. (1984) and the steepness-dependent
 177 coefficient governing dissipation by whitecapping is a linear function of the
 178 wave number. In this study, this steepness-dependent coefficient is a quadratic
 179 function of the wave number, as it showed better predictions of the significant
 180 wave height in the study of Siadatmousavi et al. (2011). The choice of these
 181 formulations was motivated by the appearance of numerical instabilities in
 182 the region of the Gulf Stream when using SWAN's default parameter values.
 183 Finally, wave boundary conditions were derived from WAVEWATCH III
 184 (Tolman et al., 2009) spectral outputs at buoy locations *[justify why]*.

185 Surface waves induce a net drift in the direction of the wave propagation,
 186 known as the Stokes drift (Van Den Bremer and Breivik, 2018; Stokes,
 187 1880). This net drift has a significant impact on sediment transport in
 188 nearshore regions (Hoefel and Elgar, 2003), on the formation of Langmuir
 189 cells (Langmuir, 1938; Craik and Leibovich, 1976) as well as on the transport
 190 of heat, salt or pollutants such as oil or micro-plastic in the upper ocean layer
 191 (McWilliams and Sullivan, 2000; Röhrs et al., 2012; Drivedal et al., 2014). To
 192 correctly model the Stokes drift profile in mixed wind-driven sea and swell
 193 conditions, the full two-dimensional wave spectrum must be represented by
 194 a spectral wave model within a wave-current coupling (Van Den Bremer and
 195 Breivik, 2018). In this study, the depth-averaged Stokes drift was therefore
 196 computed by SWAN using the following formula:

$$\mathbf{u}_s = \int_0^{2\pi} \int_0^{+\infty} \frac{\sigma^3}{h \tanh(2kh)} E(\sigma, \theta) (\cos \theta, \sin \theta) d\sigma d\theta , \quad (6)$$

197 where k is the norm of the wave vector; h is the water depth; and $E(\sigma, \theta)$ is
 198 the wave energy density.

199 *2.5. Coupled model*

200 SLIM and SWAN are coupled so that they run on the same computational
201 core and the same unstructured mesh. SLIM is run first and passes computed
202 wind velocities (\mathbf{U}_{10}), water levels ($\eta = H - h$) and depth-averaged currents
203 ($\mathbf{u} = \mathbf{U}/H$) to SWAN, as well as a roughness length (z_0) for the bottom
204 dissipation formulation of Madsen et al. (1989). This roughness length is
205 computed from SLIM's bulk drag coefficient C_b following the approach of
206 Dietrich et al. (2011) so that both models have consistent bottom dissipation
207 parameterizations. SWAN then uses these quantities to compute the wave
208 radiation stress gradient, that is then passed to SLIM as the force exerted
209 by waves on currents $\boldsymbol{\tau}_{\text{wave}}$ (Fig. 2) [*+mention we use wind-stress, not wave-*
210 *dissipative stress*]. SLIM then uses this quantity to update the the value of
211 the surface stress $\boldsymbol{\tau}_s$ in Eq. (1), that now becomes the sum of wind and
212 wave-induced stresses $\boldsymbol{\tau}_s = \boldsymbol{\tau}_{\text{wind}} + \boldsymbol{\tau}_{\text{wave}}$ [*mention vortex-force formalism and*
213 *why we chose radiation stress gradient*].

214 SLIM's governing equations are integrated using an implicit time inte-
215 gration scheme while SWAN is unconditionally stable (*say that you use the*
216 *steady version, explain the difference with the unsteady version*) (Dietrich
217 et al., 2010), allowing both models to be run with relatively large time steps.
218 In this study, both models were therefore run sequentially using a time step
219 of 600s, so that each computational core was alternating running either SLIM
220 or SWAN. As in the coupling between SWAN and ADCIRC (Dietrich et al.,
221 2010), both models utilize the same local sub-mesh, allowing for a one-to-one
222 correspondence between the geographic locations of the mesh vertices. No
223 interpolation is therefore needed when passing the discretised variables from
224 one model to the other, which allows an efficient inter-model communication.
225 However, as SLIM applies discontinuous Galerkin finite element methods,
226 an additional conversion step to a continuous framework was required to
227 transmit SLIM nodal quantities to SWAN.

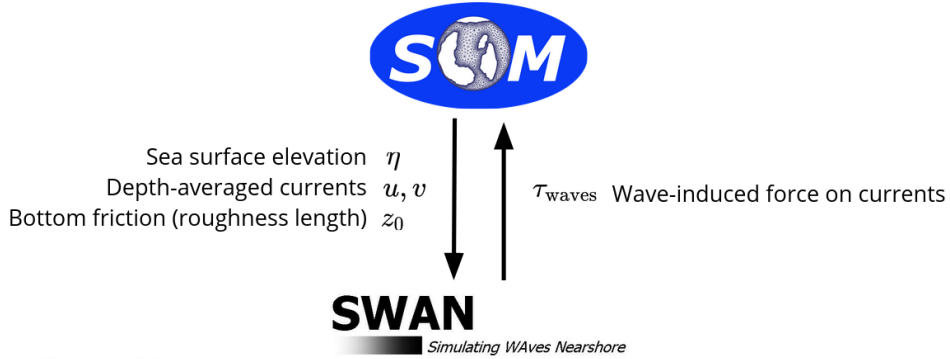


Fig. 2: Schematic illustration of the coupled SLIM+SWAN model [add U10 to diagram].

228 3. Results

229 We first validated the reconstructed atmospheric fields of hurricane Irma
 230 as well the modelled currents and waves of our coupled model against fields
 231 measurements. We then use the validated model to simulate the transport
 232 of passive drifters in the Lower Keys during the passage of Hurricane Irma.
 233 These drifters were advected by two sets of currents: (i) the currents from an
 234 uncoupled SLIM simulation of Irma (SLIM) and (ii) the currents modelled by
 235 the coupled SLIM+SWAN model (SLIM+SWAN). Furthermore, the depth-
 236 averaged Stokes drift was computed using our coupled model (Stokes_C)
 237 and an uncoupled SWAN simulation of the hurricane (Stokes_U). We then
 238 simulated the trajectories of passive tracers during the passage of the Irma in
 239 the Lower Keys using different combinations of these fields. These trajectories
 240 were finally compared to evaluate the impact of the wave-current interactions
 241 and the Stokes drift on the transport processes during a major hurricane.

242 3.1. Model validation

243 H*Wind winds and hybrid pressure field agree well with station mea-
 244 surements at Vaca Key station (Fig. 3). The hybrid pressure field shows
 245 better agreement with observations than ERA-5 pressure as it successfully
 246 reproduces the storm depression. ERA-5 fields, on the other hand, fail to

Validation of atmospheric forcings at Vaca Key station

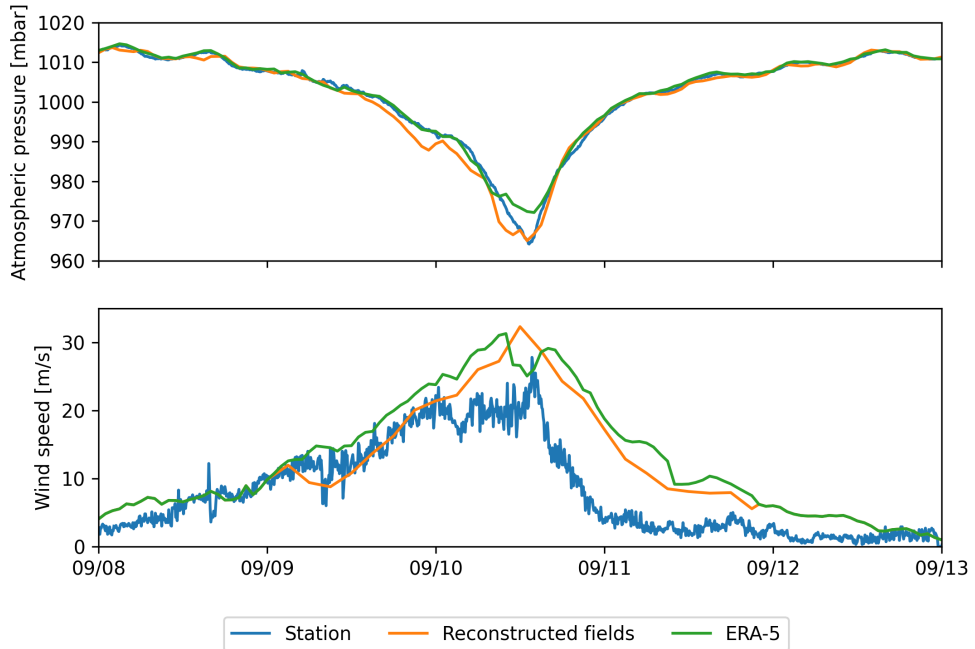


Fig. 3: Comparison of reconstructed wind atmospheric pressure with field measurements and coarser ECMWF ERA-5 profiles at Vaca Key station. The generated hybrid atmospheric forcings better capture the observed storm depression while H*wind winds better match the measured peak in wind speed.

247 resolve the low pressure at the core of the hurricane due to their coarser
 248 grid, leading to an overestimation of 8 mbar of the storm depression. Both
 249 H*Wind and ERA-5 agree well with observed wind speeds although both
 250 data sets tend to slightly overestimate the width and intensity of the wind
 251 peak. However, H*wind profiles show a better match with the timing of the
 252 observed peak, as ERA-5 winds tend to anticipate it. H*wind also exhibits a
 253 slightly narrower peak in wind speed, which better agrees with observations.

254 Hydrodynamic outputs of the coupled wave-current model agree well with
 255 tide gauge (Fig. 4) and ADCP measurements (Fig. 5). The timing and
 256 amplitude of the storm surges are well reproduced by the coupled model,
 257 the largest model error being an overestimation of 18 cm of the elevation

peak at Virginia Key. The fit is especially good at Naples, where both the large positive and negative surges are captured by the coupled model with an error of less than 5 cm. This result is of interest as negative surges, although less studied, affect water exchanges between the estuaries and the coastal ocean and disturb the benthic ecosystems (Liu et al., 2020). Modelled 2D currents were validated against depth-averaged ADCP measurements at mooring station C10, C12 and C13 (Fig. 5). As in Liu et al. (2020), we performed the vector correlation analysis of Kundu (1976) to compare modelled and observed current velocity vectors. Correlation coefficients (ρ) between simulated and observed depth-averaged currents were 0.84, 0.74 and 0.73 at the C10, C12 and C13 locations, respectively. Average veering angles were computed as well and were below 12°, as in (Liu et al., 2020). However, in our case, no clear tendency regarding modelled current behavior compared to observations was observed. As expected from a depth-averaged model, the best fit with observations is obtained at the shallowest mooring C10, located on the 25m isobath, with an average veering angle of 6°.

The simulated significant wave height agrees well with observations on the WFS, where errors on the peak value do not exceed 5% (Fig. 6). On the eastern shelf of Florida, errors are slightly larger and reach 20%. Although the model outputs agree well with observations, a lag in significant wave height is observed for all 4 buoys. Moreover, the peak in significant wave height tends to be underestimated at buoys 41113 and 41114, located on the East Florida Shelf. Other wave parameters were better reproduced by the model on the WFS as well (see buoy 42036 in Fig. 6). This good fit on the WFS is not surprising as the parameters used for wind energy input and whitecapping dissipation were based on the calibration performed by Siadatmousavi et al. (2011) on the Northern Gulf of Mexico. Wind-induced wave growth might therefore be underestimated on the eastern shelf. Consequently, incident wave do not receive enough energy to grow after breaking on the bank boundary, leading to an underestimation of the significant wave height at the location

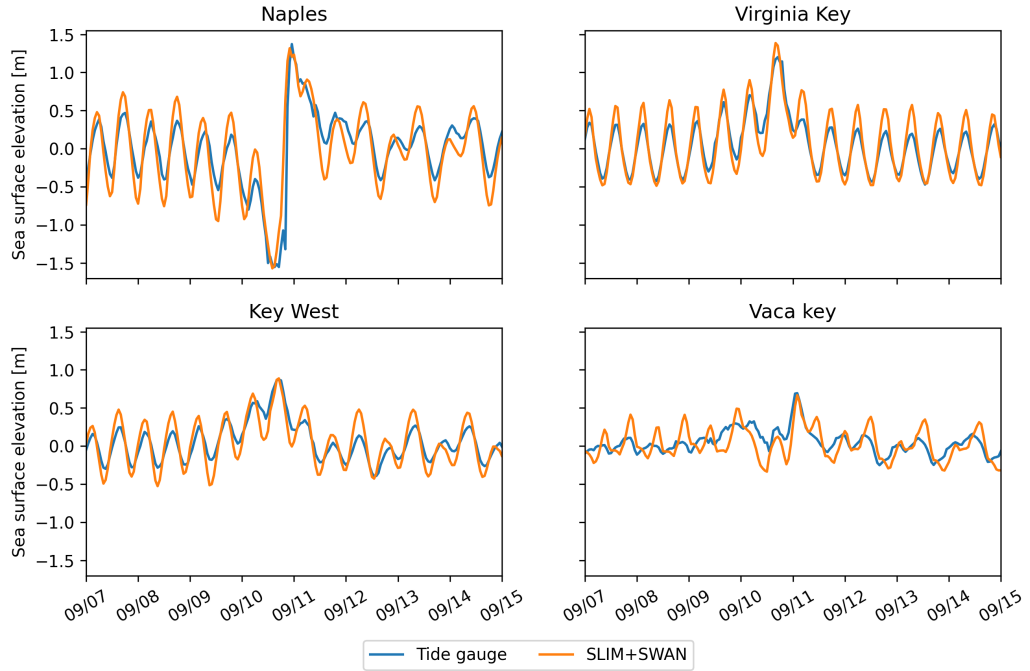


Fig. 4: Comparison of modelled sea surface elevation with all 4 tide gauge measurements (see Fig. 1B for their location). Timing and amplitudes of the storm surges are well reproduced by the model

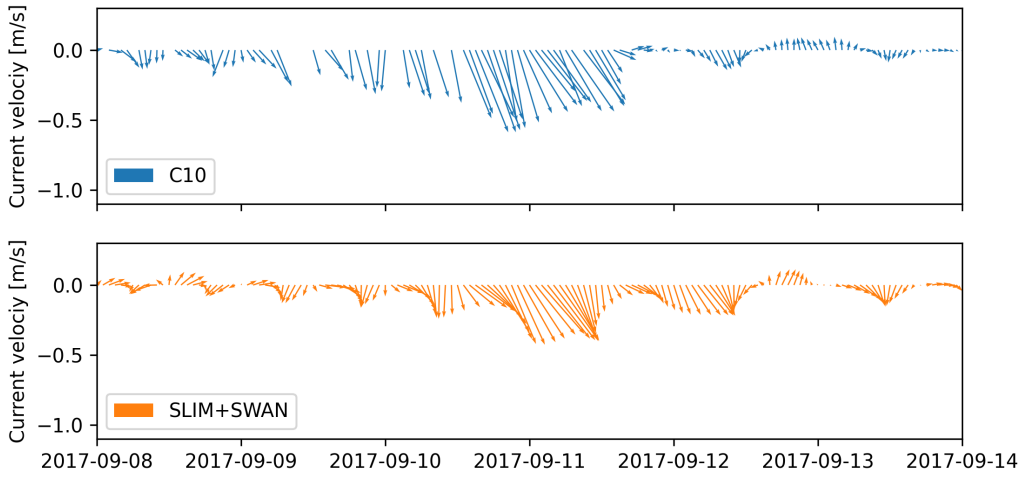


Fig. 5: Comparison of modelled current velocity with observed velocity at mooring C10 (see Fig. 1B for its location). Modelled current velocities agree well with observations, with a correlation coefficient of 0.83 and an average veering angle of 6° .

288 of the buoys. Nonetheless, as this study focused on the wave produced
289 by Irma, which made landfall on the western coasts of Florida, the use of
290 parameterizations calibrated for the Gulf of Mexico seems reasonable.

291 *[include error statistics (e.g. mean bias, absolute error, and RMSE) +
292 present them in a table]*

293 *3.2. Impact of waves on currents and transport* [Add dispersion analysis]

294 We evaluated the impact of wave-current interactions on modelled currents
295 during the passage of Irma in the Lower Keys, between Sept. 7 and 13, 2017.
296 First, we computed the maximum difference between currents modelled by
297 SLIM and SLIM+SWAN during this period (Fig. 7A). The largest differences
298 in current speed were observed over the reefs, on the shelf break and around
299 islands. They can locally reach 1 m/s, with the coupled model SLIM+SWAN
300 yielding the largest amplitudes. The regions where the differences are the
301 largest experience the largest wave-induced stress τ_{wave} (Fig. 7B), as wave
302 breaking and wave slowing down over rough seabed induce variations of the
303 wave radiation stress (Longuet-Higgins and Stewart, 1964). Wave-induced
304 differences in current speed were amplified by the action of the wind stress
305 τ_{wind} (Fig. 7C). Wind speeds were larger in the front right quadrant of the
306 hurricane (Zedler et al., 2009), yielding larger differences on the right-hand
307 side of the storm trajectory. This is especially clear in the area between
308 the Florida Keys and the Everglades, where relatively small values of τ_{wave}
309 nonetheless produce current speed differences of up to 0.5 m/s because of the
310 wind stress.

311 To quantify the impact of these differences in the velocity fields, we
312 compared the trajectories of passive particles advected by the uncoupled
313 SLIM and coupled SLIM+SWAN currents during the passage of Irma in the
314 Lower Keys (Fig. 8). Particles were released on the inner and outer shelves
315 at the points highlighted in red and blue dots in Fig. 8A on 7 September
316 and then tracked until 15 September. These areas were constructed using
317 backtracking methods (Dobbelaeere et al., 2020a) to ensure that the release

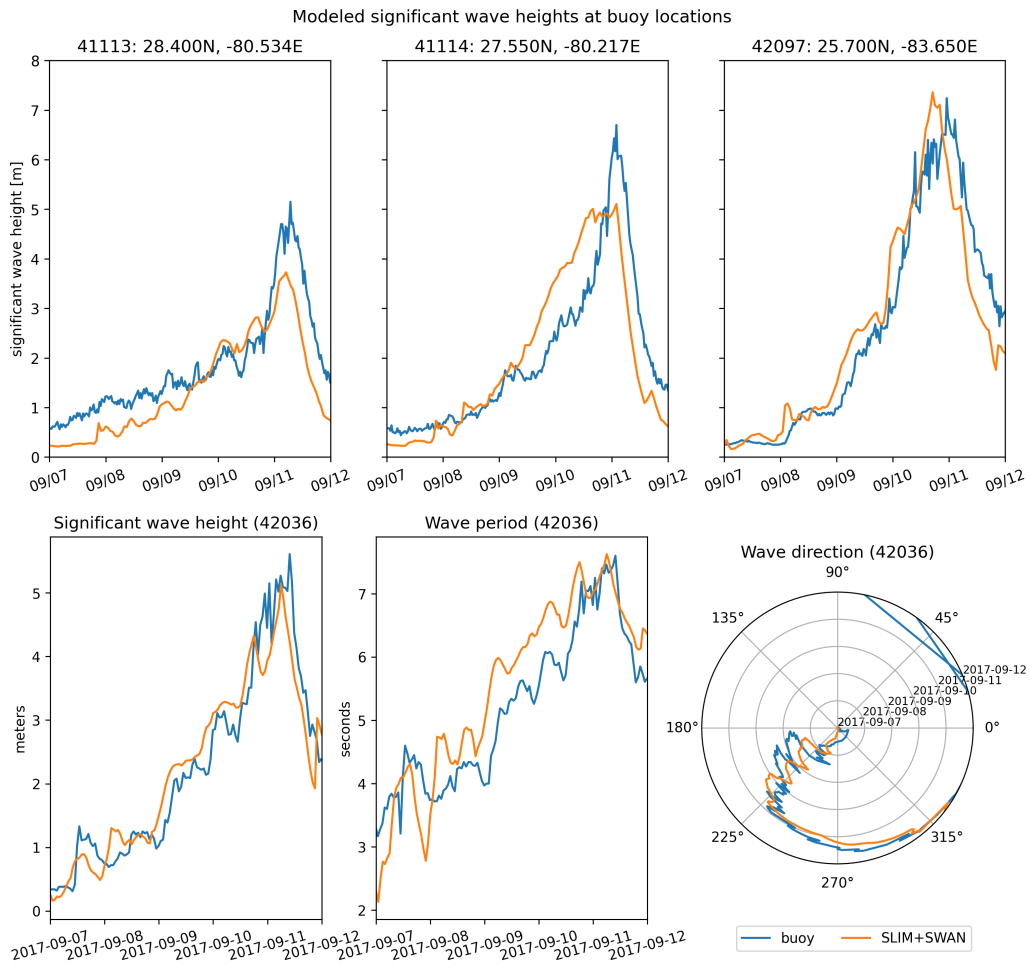


Fig. 6: Comparison of modelled wave parameters with observation at the 4 buoys location (locations shown in Fig. 1B). Modelled significant wave height agrees well with field measurement. As model parameters were calibrated for the Northern Gulf of Mexico, observations are better reproduced at buoys located on the WFS, as illustrated for buoy 42036

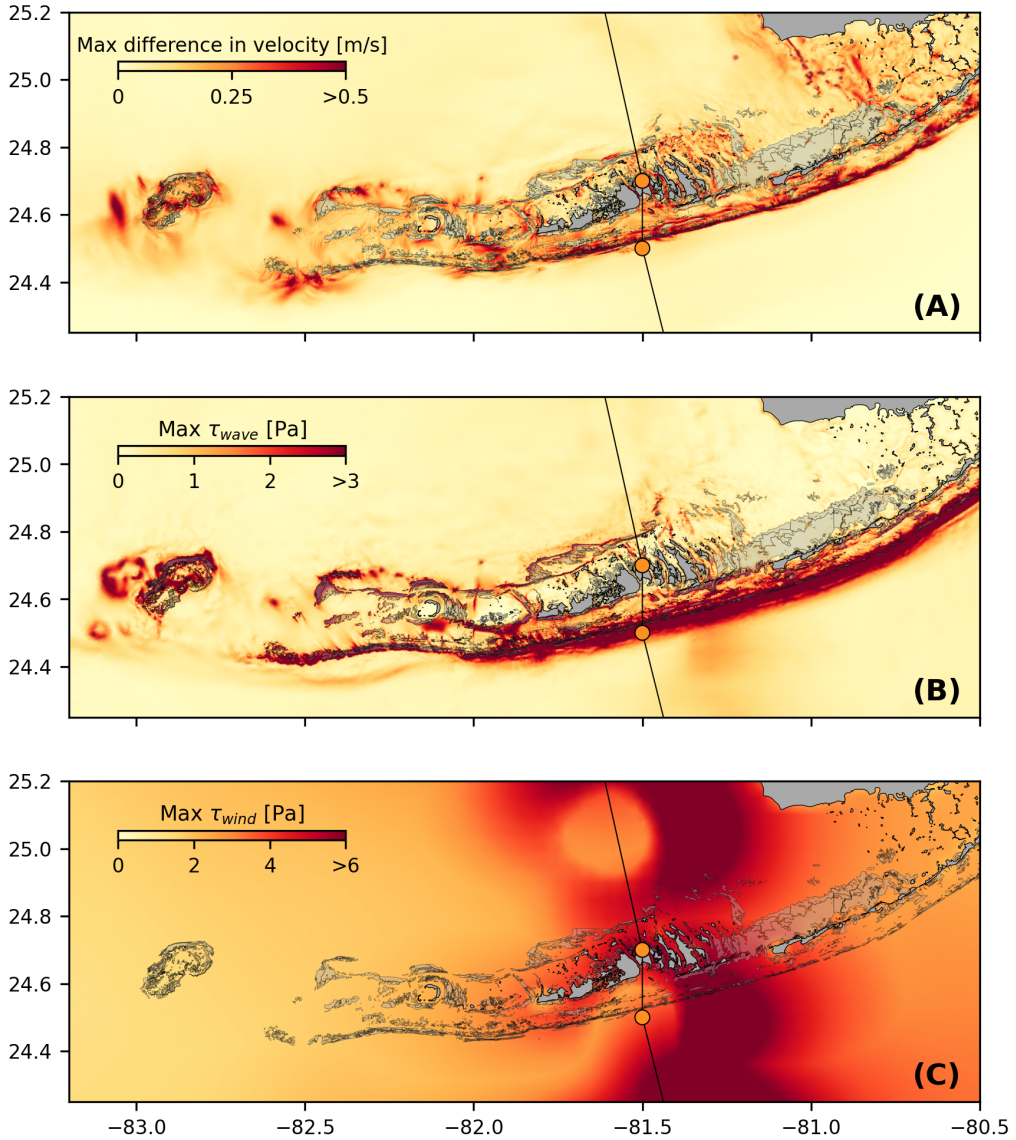


Fig. 7: Maximum difference between SLIM and SLIM+SWAN currents (A) during the passage of Irma in the Lower Florida Keys, along with the maximum wave radiation stress gradient τ_{wave} (B) and wind stress τ_{wind} (C) generated by the hurricane. Wave-induced stress yields difference larger than 0.5 m/s in current velocities. These wave-induced differences in currents were amplified by the action of the asymmetric wind profile of Irma, with larger differences occurring on the right of the storm trajectory

318 particles would intersect the path of Irma during its passage in the Florida
319 Keys. We first defined two 25km^2 circular regions on the trajectory of the
320 hurricane (see red and blue circles in Fig. 8A). Particles within these two
321 regions were then tracked backward in time using uncoupled SLIM currents
322 from the exact time of the passage of the hurricane until the 7th of September.
323 Their positions at the end of the backward simulation (see red and blue
324 particle clouds in Fig. 8) corresponds to the initial condition of the forward
325 transport simulations described below.

326 We compared the trajectories of particles originating from these regions
327 and advected forward in time by different sets of currents: (i) uncoupled SLIM
328 currents alone; (ii) coupled SLIM+SWAN currents; (iii) SLIM currents with
329 the addition of the depth-averaged Stokes drift computed by the coupled wave
330 model (Stokes_C); (iv) SLIM+SWAN currents with Stokes_C; and (v) SLIM
331 currents with the depth-averaged Stokes drift computed by the uncoupled
332 wave model (Stokes_U). Particles trajectories are compared by computing
333 the distances between the centers of mass of the particle clouds through
334 time. Here are our main observations (*this needs to be improved, feedback is
335 welcome!*) :

- 336 • The impact of wave-current interactions is the most important during the
337 passage of the hurricane but negligible during the rest of the simulated
338 period. This is clear when comparing the clouds of particles advected
339 by SLIM and SLIM+SWAN on the outer shelf [plot clouds of particles
340 to make it clearer]. The distance between the centers of mass reaches 5
341 km during the passage of Irma but is negligible during the rest of the
342 simulated period.
- 343 • The impact of the Stokes drift is larger than the impact of the wave-
344 current interactions on the inner shelf. The difference between the
345 centers of mass does not exceed ~ 1 km for SLIM vs SLIM+SWAN but
346 reaches about 5 km for SLIM vs SLIM+Stokes_C and SLIM+SWAN+Stokes_C.
347 On the outer shelf, the currents are more intense and the impact the

348 wave-current coupling during the passage of the hurricane is sufficient
349 to generate a difference between the two clouds of particles that keeps
350 on increasing after the passage of the hurricane. The impact of the
351 Stokes drift remains however larger than the impact of the wave-current
352 coupling. This difference between the inner and outer shelf can be
353 explained by the sheltering of the inner shelf due to reefs and islands
354 as well as wave breaking on the shelf break. The inner shelf hence
355 experiences weaker waves and weaker currents, and hence also weaker
356 and more localised transport.

- 357 • On the inner shelf, the distance between the centers of mass of the
358 particle clouds stabilizes after the passage of the hurricane while this
359 distance keeps increasing during a couple of days after the passage of
360 the hurricane on the outer shelf under the action of the Stokes drift.
361 This shows the strong impact of wave-induced transport in the open
362 ocean.
- 363 • Impact of Stokes drift and wave-current interactions weaker on the inner
364 shelf. Max. distance of about 5 km between the centers of mass of the
365 clouds of particles compared to 30km on the outer shelves
- 366 • The fact that SLIM+Stokes_C vs. SLIM+Stokes_U keeps increasing on
367 the outer shelf after the passage of the hurricane shows the impact of
368 the strong current velocities of the FC on the modelled Stokes drift
- 369 • Nonetheless, the differences between the coupled and uncoupled Stokes
370 drifts remains relatively small with a maximum value of 2 km between
371 the centers of mass of the simulated particle clouds. Furthermore, as
372 SLIM vs SLIM+SWAN+Stokes and SLIM vs. SLIM+Stokes_C show
373 similar values on the inner shelf, this suggests that the combination
374 of currents and Stokes drifts produces sufficiently accurate results on
375 sheltered shallow areas such as the WFS. However, neglecting the wave-

376 current interactions leads to differences of up to 5 km in modelled
377 particle trajectories on the outer shelf.

- 378
- 379 • Matthieu: Pour la partie discussion, je pense que tu peux essayer de
380 mettre en avant un des avantages du modle, qui est la haute rsolution
381 entre les les des Keys (en plus du couplage avec les vagues). Je pense
382 que a peut faire partie de "impact of waves on coral connectivity" que
tu mentionnes dans ta partie 4.

383 *[Milan: Two first points could be well summarized in table --]*

384 **4. Discussion**

385 Impact of waves on coral connectivity

386 Ability of wave model to correctly capture gradient in significant wave
387 height due to current-waves interactions under tropical cyclones depends on:

- 388
- 389 • Broad perspective \Rightarrow not limited to FL
 - 390 • Mention search and rescue
 - 391 • However, ignoring waves in storm conditions could result in significant
392 inaccuracies in modelled trajectories, as illustrated in the case of release
region 2 in Fig. 8
 - 393 • Spatial (10km \rightarrow 5km) and spectral (36 dir. \rightarrow 48 dir.) resolution
394 (Hegermiller et al., 2019)
 - 395 • Directional spreading of incident waves (Villas Bôas et al., 2020)

396 **5. Conclusion**

397 **Acknowledgments**

398 Computational resources were provided by the Consortium des Équipements
399 de Calcul Intensif (CÉCI), funded by the F.R.S.-FNRS under Grant No.

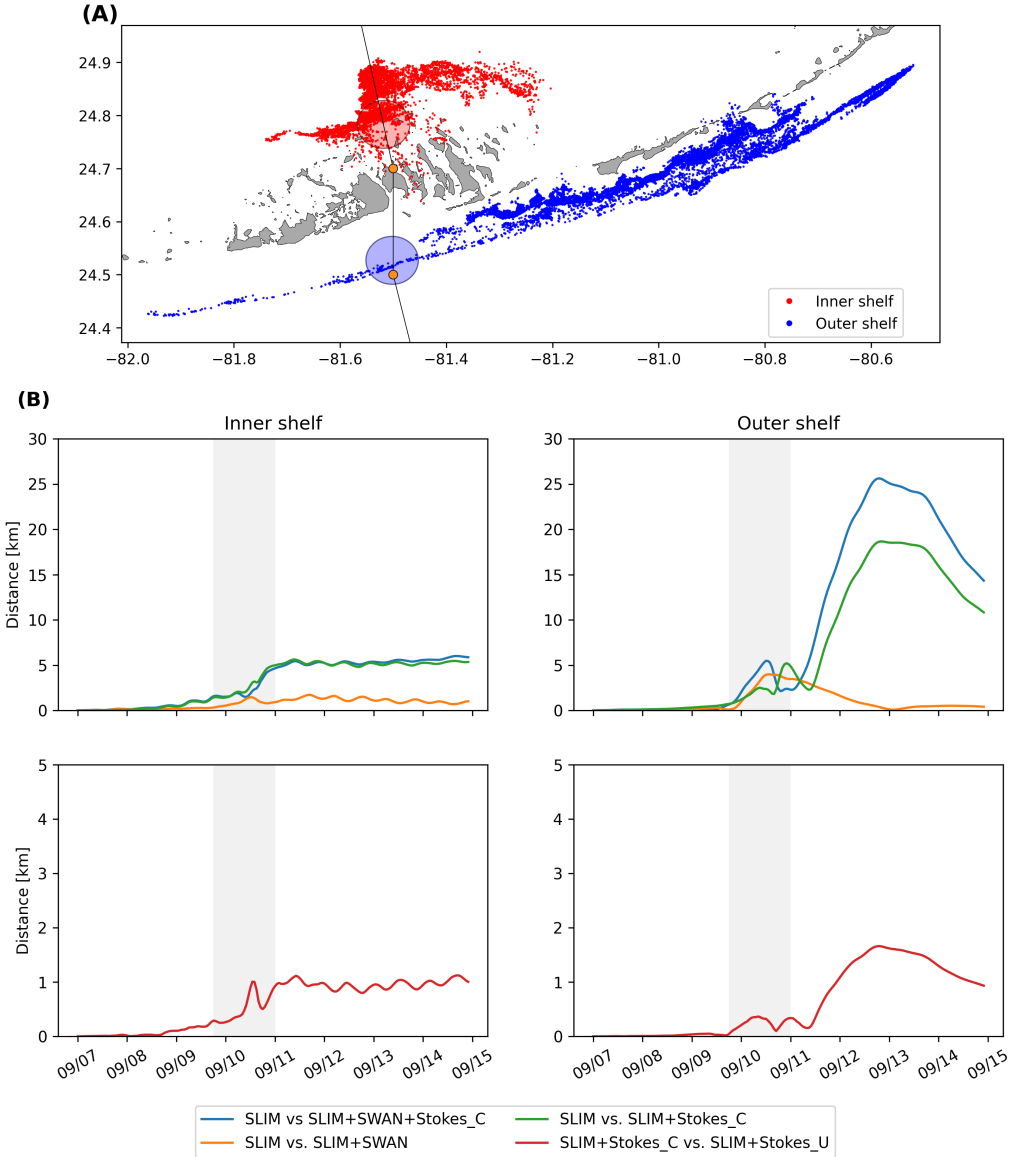


Fig. 8: **A:** Release regions of the passive particles on the inner and outer shelves (red and blue clouds) obtained by backtracking particles released in the red and blue circular areas during the passage of Irma. **B:** Difference between the centers of mass of the particle clouds released from the regions highlighted in **A** and advected by different combinations of coupled and uncoupled velocity fields. **Matthieu: prsenter plus d'informations sur la Figure 8, notamment les nuages de points issus des deux simulations (SLIM et SLIM+SWAN+Stokes_C), ainsi que les centres de masses correspondants. Ca devrait permettre de soutenir la partie rsultats.**

400 2.5020.11. Thomas Dobbelaere is a PhD student supported by the Fund for
401 Research training in Industry and Agriculture (FRIA/FNRS).

402 **References**

- 403 Bever, A.J., MacWilliams, M.L., 2013. Simulating sediment transport pro-
404 cesses in San Pablo Bay using coupled hydrodynamic, wave, and sediment
405 transport models. *Marine Geology* 345, 235–253.
- 406 Booij, N., Ris, R.C., Holthuijsen, L.H., 1999. A third-generation wave
407 model for coastal regions: 1. Model description and validation. *Journal of*
408 *geophysical research: Oceans* 104, 7649–7666.
- 409 Chassignet, E.P., Hurlbert, H.E., Smedstad, O.M., Halliwell, G.R., Hogan,
410 P.J., Wallcraft, A.J., Baraille, R., Bleck, R., 2007. The HYCOM (hybrid
411 coordinate ocean model) data assimilative system. *Journal of Marine*
412 *Systems* 65, 60–83.
- 413 Chen, C., Huang, H., Beardsley, R.C., Liu, H., Xu, Q., Cowles, G., 2007.
414 A finite volume numerical approach for coastal ocean circulation studies:
415 Comparisons with finite difference models. *Journal of Geophysical Research:*
416 *Oceans* 112.
- 417 Craik, A.D., Leibovich, S., 1976. A rational model for Langmuir circulations.
418 *Journal of Fluid Mechanics* 73, 401–426.
- 419 Curcic, M., Chen, S.S., Özgökmen, T.M., 2016. Hurricane-induced ocean
420 waves and stokes drift and their impacts on surface transport and dispersion
421 in the Gulf of Mexico. *Geophysical Research Letters* 43, 2773–2781.
- 422 Curcic, M., Haus, B.K., 2020. Revised estimates of ocean surface drag in
423 strong winds. *Geophysical Research Letters* 47, e2020GL087647.

- 424 Dietrich, J., Bunya, S., Westerink, J., Ebersole, B., Smith, J., Atkinson,
425 J., Jensen, R., Resio, D., Luettich, R., Dawson, C., et al., 2010. A high-
426 resolution coupled riverine flow, tide, wind, wind wave, and storm surge
427 model for southern louisiana and mississippi. part ii: Synoptic description
428 and analysis of hurricanes katrina and rita. Monthly Weather Review 138,
429 378–404.
- 430 Dietrich, J., Westerink, J., Kennedy, A., Smith, J., Jensen, R., Zijlema, M.,
431 Holthuijsen, L., Dawson, C., Luettich, R., Powell, M., et al., 2011. Hurricane
432 gustav (2008) waves and storm surge: Hindcast, synoptic analysis, and
433 validation in southern louisiana. Monthly Weather Review 139, 2488–2522.
- 434 Dobbelaere, T., Muller, E., Gramer, L., Holstein, D., Hanert, E., 2020a.
435 Report on the potential origin of the SCTLD in the Florida Reef Tract.
436 Available online at: <https://floridadep.gov/rcp/coral/documents/report-potential-origin-sctld-florida-reef-tract>.
- 438 Dobbelaere, T., Muller, E.M., Gramer, L.J., Holstein, D.M., Hanert, E., 2020b.
439 Coupled epidemi-hydrodynamic modeling to understand the spread of a
440 deadly coral disease in Florida. Frontiers in Marine Science 7, 1016.
- 441 Donelan, M., Haus, B., Reul, N., Plant, W., Stiassnie, M., Gruber, H., Brown,
442 O., Saltzman, E., 2004. On the limiting aerodynamic roughness of the
443 ocean in very strong winds. Geophysical Research Letters 31.
- 444 Drivdal, M., Broström, G., Christensen, K., 2014. Wave-induced mixing and
445 transport of buoyant particles: application to the statfjord a oil spill. Ocean
446 Science 10, 977–991.
- 447 Figueiredo, J., Baird, A.H., Connolly, S.R., 2013. Synthesizing larval com-
448 petence dynamics and reef-scale retention reveals a high potential for
449 self-recruitment in corals. Ecology 94, 650–659.

- 450 Frys, C., Saint-Amand, A., Le Hénaff, M., Figueiredo, J., Kuba, A., Walker,
451 B., Lambrechts, J., Vallaeyns, V., Vincent, D., Hanert, E., 2020. Fine-scale
452 coral connectivity pathways in the Florida Reef Tract: implications for
453 conservation and restoration. *Frontiers in Marine Science* 7, 312.
- 454 Geuzaine, C., Remacle, J.F., 2009. Gmsh: A 3-d finite element mesh generator
455 with built-in pre-and post-processing facilities. *International journal for
456 numerical methods in engineering* 79, 1309–1331.
- 457 Harper, B., Kepert, J., Ginger, J., 2010. Guidelines for converting between
458 various wind averaging periods in tropical cyclone conditions. Citeseer.
- 459 Hegermiller, C.A., Warner, J.C., Olabarrieta, M., Sherwood, C.R., 2019.
460 Wave-current interaction between Hurricane Matthew wave fields and the
461 Gulf Stream. *Journal of Physical Oceanography* 49, 2883–2900.
- 462 Hoefel, F., Elgar, S., 2003. Wave-induced sediment transport and sandbar
463 migration. *Science* 299, 1885–1887.
- 464 Hoffmeister, J., Multer, H., 1968. Geology and origin of the Florida Keys.
465 Geological Society of America Bulletin 79, 1487–1502.
- 466 Holthuijsen, L.H., Powell, M.D., Pietrzak, J.D., 2012. Wind and waves in
467 extreme hurricanes. *Journal of Geophysical Research: Oceans* 117.
- 468 Janssen, P.A., 1991. Quasi-linear theory of wind-wave generation applied to
469 wave forecasting. *Journal of physical oceanography* 21, 1631–1642.
- 470 Johns, W.E., Schott, F., 1987. Meandering and transport variations of the
471 Florida Current. *Journal of physical oceanography* 17, 1128–1147.
- 472 Knaff, J.A., Sampson, C.R., Musgrave, K.D., 2018. Statistical tropical cyclone
473 wind radii prediction using climatology and persistence: Updates for the
474 western North Pacific. *Weather and Forecasting* 33, 1093–1098.

- 475 Knutson, T.R., McBride, J.L., Chan, J., Emanuel, K., Holland, G., Landsea,
476 C., Held, I., Kossin, J.P., Srivastava, A., Sugi, M., 2010. Tropical cyclones
477 and climate change. *Nature geoscience* 3, 157–163.
- 478 Komen, G., Hasselmann, S., Hasselmann, K., 1984. On the existence of a
479 fully developed wind-sea spectrum. *Journal of physical oceanography* 14,
480 1271–1285.
- 481 Kourafalou, V.H., Kang, H., 2012. Florida Current meandering and evo-
482 lution of cyclonic eddies along the Florida Keys Reef Tract: Are they
483 interconnected? *Journal of Geophysical Research: Oceans* 117.
- 484 Kundu, P.K., 1976. Ekman veering observed near the ocean bottom. *Journal*
485 *of Physical Oceanography* 6, 238–242.
- 486 Landsea, C.W., Franklin, J.L., 2013. Atlantic hurricane database uncertainty
487 and presentation of a new database format. *Monthly Weather Review* 141,
488 3576–3592.
- 489 Langmuir, I., 1938. Surface motion of water induced by wind. *Science* 87,
490 119–123.
- 491 Le Hénaff, M., Kourafalou, V.H., Paris, C.B., Helgers, J., Aman, Z.M., Hogan,
492 P.J., Srinivasan, A., 2012. Surface evolution of the Deepwater Horizon
493 oil spill patch: combined effects of circulation and wind-induced drift.
494 *Environmental science & technology* 46, 7267–7273.
- 495 Lee, T.N., Leaman, K., Williams, E., Berger, T., Atkinson, L., 1995. Florida
496 Current meanders and gyre formation in the southern Straits of Florida.
497 *Journal of Geophysical Research: Oceans* 100, 8607–8620.
- 498 Lee, T.N., Mayer, D.A., 1977. Low-frequency current variability and spin-off
499 eddies along the shelf off southeast Florida. *Collected Reprints* 1, 344.

- 500 Lee, T.N., Smith, N., 2002. Volume transport variability through the Florida
501 Keys tidal channels. *Continental Shelf Research* 22, 1361–1377.
- 502 Lee, T.N., Williams, E., 1988. Wind-forced transport fluctuations of the
503 Florida Current. *Journal of Physical Oceanography* 18, 937–946.
- 504 Li, Z., Johns, B., 1998. A three-dimensional numerical model of surface
505 waves in the surf zone and longshore current generation over a plane beach.
506 *Estuarine, Coastal and Shelf Science* 47, 395–413.
- 507 Lidz, B.H., Shinn, E.A., 1991. Paleoshorelines, reefs, and a rising sea: South
508 florida, usa. *Journal of Coastal Research* , 203–229.
- 509 Lin, N., Chavas, D., 2012. On hurricane parametric wind and applications in
510 storm surge modeling. *Journal of Geophysical Research: Atmospheres* 117.
- 511 Liu, Y., Weisberg, R.H., 2012. Seasonal variability on the West Florida shelf.
512 *Progress in Oceanography* 104, 80–98.
- 513 Liu, Y., Weisberg, R.H., Zheng, L., 2020. Impacts of hurricane Irma on the
514 circulation and transport in Florida Bay and the Charlotte Harbor estuary.
515 *Estuaries and Coasts* 43, 1194–1216.
- 516 Liubartseva, S., Coppini, G., Lecci, R., Clementi, E., 2018. Tracking plastics
517 in the Mediterranean: 2D Lagrangian model. *Marine pollution bulletin*
518 129, 151–162.
- 519 Longuet-Higgins, M.S., 1970. Longshore currents generated by obliquely
520 incident sea waves. *Journal of geophysical research* 75, 6778–6789.
- 521 Longuet-Higgins, M.S., Stewart, R., 1964. Radiation stresses in water waves;
522 a physical discussion, with applications, in: Deep sea research and oceano-
523 graphic abstracts, Elsevier. pp. 529–562.
- 524 Madsen, O.S., Poon, Y.K., Gruber, H.C., 1989. Spectral wave attenuation by
525 bottom friction: Theory, in: *Coastal Engineering* 1988, pp. 492–504.

- 526 Malmstadt, J., Scheitlin, K., Elsner, J., 2009. Florida hurricanes and damage
527 costs. *southeastern geographer* 49, 108–131.
- 528 Marsooli, R., Lin, N., Emanuel, K., Feng, K., 2019. Climate change ex-
529 acerbates hurricane flood hazards along US Atlantic and Gulf Coasts in
530 spatially varying patterns. *Nature communications* 10, 1–9.
- 531 McWilliams, J.C., Sullivan, P.P., 2000. Vertical mixing by Langmuir circula-
532 tions. *Spill Science & Technology Bulletin* 6, 225–237.
- 533 Mei, C.C., 1989. The applied dynamics of ocean surface waves. volume 1.
534 World scientific.
- 535 Moon, I.J., Ginis, I., Hara, T., Thomas, B., 2007. A physics-based parame-
536 terization of air-sea momentum flux at high wind speeds and its impact on
537 hurricane intensity predictions. *Monthly weather review* 135, 2869–2878.
- 538 Pinelli, J.P., Roueche, D., Kijewski-Correa, T., Plaz, F., Prevatt, D., Zisis,
539 I., Elawady, A., Haan, F., Pei, S., Gurley, K., et al., 2018. Overview of
540 damage observed in regional construction during the passage of Hurricane
541 Irma over the State of Florida, in: *Forensic Engineering 2018: Forging*
542 *Forensic Frontiers*. American Society of Civil Engineers Reston, VA, pp.
543 1028–1038.
- 544 Powell, M.D., Houston, S.H., Amat, L.R., Morisseau-Leroy, N., 1998. The
545 HRD real-time hurricane wind analysis system. *Journal of Wind Engineering*
546 and Industrial Aerodynamics 77, 53–64.
- 547 Powell, M.D., Vickery, P.J., Reinhold, T.A., 2003. Reduced drag coefficient
548 for high wind speeds in tropical cyclones. *Nature* 422, 279–283.
- 549 Röhrs, J., Christensen, K.H., Hole, L.R., Broström, G., Drivdal, M., Sundby,
550 S., 2012. Observation-based evaluation of surface wave effects on currents
551 and trajectory forecasts. *Ocean Dynamics* 62, 1519–1533.

- 552 Schott, F.A., Lee, T.N., Zantopp, R., 1988. Variability of structure and
553 transport of the Florida Current in the period range of days to seasonal.
554 *Journal of Physical Oceanography* 18, 1209–1230.
- 555 Shinn, E.A., 1988. The geology of the Florida Keys. *Oceanus* 31, 46–53.
- 556 Siadatmousavi, S.M., Jose, F., Stone, G., 2011. Evaluation of two WAM
557 white capping parameterizations using parallel unstructured SWAN with
558 application to the Northern Gulf of Mexico, USA. *Applied Ocean Research*
559 33, 23–30.
- 560 Sikirić, M.D., Roland, A., Janečković, I., Tomazić, I., Kuzmić, M., 2013.
561 Coupling of the Regional Ocean Modeling System (roms) and Wind Wave
562 Model. *Ocean Modelling* 72, 59–73.
- 563 Smith, N.P., 1982. Response of Florida Atlantic shelf waters to hurricane
564 David. *Journal of Geophysical Research: Oceans* 87, 2007–2016.
- 565 Stokes, G.G., 1880. On the theory of oscillatory waves. *Transactions of the*
566 *Cambridge philosophical society* .
- 567 Tolman, H.L., et al., 2009. User manual and system documentation of
568 WAVEWATCH III TM version 3.14. Technical note, MMAB Contribution
569 276, 220.
- 570 Van Den Bremer, T., Breivik, Ø., 2018. Stokes drift. *Philosophical Transactions of the Royal Society A: Mathematical, Physical and Engineering Sciences* 376, 20170104.
- 573 Villas Bôas, A.B., Cornuelle, B.D., Mazloff, M.R., Gille, S.T., Arduin, F.,
574 2020. Wave-current interactions at meso-and submesoscales: Insights from
575 idealized numerical simulations. *Journal of Physical Oceanography* 50,
576 3483–3500.

- 577 Weisberg, R., Liu, Y., Mayer, D., 2009. Mean circulation on the west Florida
578 continental shelf observed with long-term moorings. *Geophys. Res. Lett*
579 36, L19610.
- 580 Weisberg, R.H., Zheng, L., 2006. Hurricane storm surge simulations for
581 Tampa Bay. *Estuaries and Coasts* 29, 899–913.
- 582 Wu, L., Chen, C., Guo, P., Shi, M., Qi, J., Ge, J., 2011. A FVCOM-
583 based unstructured grid wave, current, sediment transport model, I. Model
584 description and validation. *Journal of Ocean University of China* 10, 1–8.
- 585 Xian, S., Feng, K., Lin, N., Marsooli, R., Chavas, D., Chen, J., Hatzikyriakou,
586 A., 2018. Brief communication: Rapid assessment of damaged residential
587 buildings in the Florida Keys after Hurricane Irma. *Natural Hazards and*
588 *Earth System Sciences* 18, 2041–2045.
- 589 Zedler, S., Niiler, P., Stammer, D., Terrill, E., Morzel, J., 2009. Ocean's
590 response to Hurricane Frances and its implications for drag coefficient
591 parameterization at high wind speeds. *Journal of Geophysical Research: Oceans* 114.
- 593 Zhang, C., Durgan, S.D., Lagomasino, D., 2019. Modeling risk of mangroves
594 to tropical cyclones: A case study of Hurricane Irma. *Estuarine, Coastal*
595 *and Shelf Science* 224, 108–116.